



**HAL**  
open science

## Optimizing one-dimensional TiO<sub>2</sub> for photocatalytic hydrogen production from a water-ethanol mixture and other electron donors

Tao Peng, Jian Zhang, Srimanta Ray, Fatemeh Saadat Ghareh Bagh, Houssam Fakhouri, Farzaneh Arefi-Khonsari, Jerald A Lalman

### ► To cite this version:

Tao Peng, Jian Zhang, Srimanta Ray, Fatemeh Saadat Ghareh Bagh, Houssam Fakhouri, et al.. Optimizing one-dimensional TiO<sub>2</sub> for photocatalytic hydrogen production from a water-ethanol mixture and other electron donors. *Journal of Environmental Chemical Engineering*, 2019, 7 (1), e102868 (10p). 10.1016/j.jece.2018.102868 . hal-02060577

**HAL Id: hal-02060577**

**<https://hal.science/hal-02060577>**

Submitted on 13 Oct 2021

**HAL** is a multi-disciplinary open access archive for the deposit and dissemination of scientific research documents, whether they are published or not. The documents may come from teaching and research institutions in France or abroad, or from public or private research centers.

L'archive ouverte pluridisciplinaire **HAL**, est destinée au dépôt et à la diffusion de documents scientifiques de niveau recherche, publiés ou non, émanant des établissements d'enseignement et de recherche français ou étrangers, des laboratoires publics ou privés.

1                   **Optimizing one-dimensional TiO<sub>2</sub> for photocatalytic hydrogen production from a**  
2                   **water-ethanol mixture and other electron donors**

3 Tao Peng<sup>a,b</sup>, Jian Zhang<sup>d</sup>, Srimanta Ray<sup>c</sup>, Fatemeh Saadat Ghareh Bagh<sup>a</sup>, Houssam Fakhouri<sup>b</sup>,  
4 Farzaneh Arefi-Khonsari<sup>b,#</sup>, Jerald A. Lalman<sup>a,##</sup>

5  
6 <sup>a</sup>Department of Civil and Environmental Engineering, University of Windsor, 401 Sunset Ave.,  
7 Windsor, Ontario N9B 3P4, Canada

8 <sup>b</sup>Laboratoire Interfaces et Systèmes Electrochimiques (LISE), Centre national de la recherche  
9 scientifique (CNRS), Sorbonne Université, Paris F-75005, France

10 <sup>c</sup>Department of Chemical Engineering, National Institute of Technology Agartala, Tripura, India,  
11 799055

12 <sup>d</sup>State Key Laboratory of Material Processing and Die and Mould Technology, School of  
13 Materials Science and Engineering, Huazhong University of Science and Technology, Wuhan  
14 430074, China

15  
16  
17  
18  
19  
20  
21  
22  
23  
24  
25  
26  
27 #Farzaneh Arefi-Khonsari, Voice: +33-144276815; Fax: +33-144276813; Email:  
28 farzaneh.arefi@upmc.fr

29 ##Jerald A. Lalman, Voice: +1-519-253-3000 ext. 2519; Fax + 1-519-971-3686; Email:  
30 lalman@uwindsor.ca

31

32 **Abstract**

33 This work is focused on synthesizing and employing one-dimensional (1D) titanium dioxide  
34 (TiO<sub>2</sub>) for hydrogen (H<sub>2</sub>) production. Based on using electron donors (EDs) (ethanol, methanol,  
35 fomic acid and 1,2,3 propanetriol), the increased H<sub>2</sub> production, when compared to P25 TiO<sub>2</sub>  
36 nanoparticles, was due to the large specific surface area (SSA) and enhanced electron mobility of  
37 1D TiO<sub>2</sub>. The impact of the 1D TiO<sub>2</sub> synthesis reaction conditions (temperature, NaOH  
38 concentration and the TiO<sub>2</sub> precursor concentration) on the photocatalytic H<sub>2</sub> production rate was  
39 evaluated using a 3-factor 3-level Box Behnken design (BBD). The BBD model demonstrated  
40 that the temperature and the NaOH concentration significantly affected the 1D TiO<sub>2</sub> phase  
41 structure, crystal size, SSA, bandgap and the photocatalytic H<sub>2</sub> production rate. The phase  
42 structure and crystal size of 1D TiO<sub>2</sub> were key factors affecting the H<sub>2</sub> production rate. 1D TiO<sub>2</sub>  
43 containing an anatase phase with a mean crystal size of 20.1±0.2 nm was synthesized at 126°C,  
44 15 M NaOH and 49 g·L<sup>-1</sup> TiO<sub>2</sub>. The maximum H<sub>2</sub> production rate of 475±12 μmol·h<sup>-1</sup> (quantum  
45 efficiency (ε) = 20.2±0.5%) for the 1D TiO<sub>2</sub> sample was significantly enhanced when compared  
46 to commercial TiO<sub>2</sub> P25. The H<sub>2</sub> production rate for the optimized 1D TiO<sub>2</sub> was significantly  
47 enhanced by decorating the structure with Pt and Au. Hydrothermal synthesized of 1D TiO<sub>2</sub>  
48 provided an efficient and low cost method for producing H<sub>2</sub> from ethanol, methanol, fomic acid  
49 and 1,2,3 propanetriol.

50

51 **Key words:** 1D titanium dioxide, photocatalyst, anatase, TiO<sub>2</sub>-B, hydrothermal, hydrogen  
52 production, quantum yield.

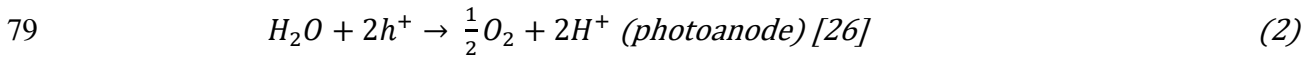
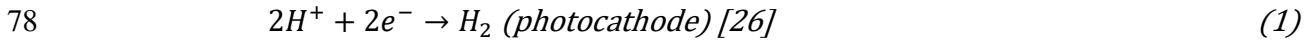
53

54 **1. Introduction**

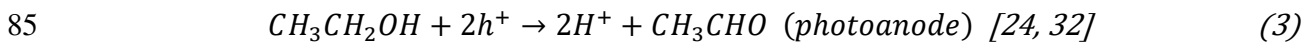
55 Hydrogen is considered as a promising fuel for the future. 1D TiO<sub>2</sub> nanomaterials have  
56 shown significant potential in producing H<sub>2</sub> because of their high electron mobility, large SSA  
57 and high mechanical strength [1-5]. Producing 1D TiO<sub>2</sub> using the alkaline hydrothermal method  
58 is a relatively facile process with advantages of large-scale production and varied crystal phase  
59 [1, 2, 4-11]. In studies employing the hydrothermal method, 1D TiO<sub>2</sub> nanomaterials containing  
60 anatase [1, 12] or TiO<sub>2</sub>-B [10, 11] were produced under selected synthesis conditions. These  
61 materials have been utilized to produce hydrogen (H<sub>2</sub>) from the photocatalytic splitting of water  
62 or from other substrates such as ethanol [10, 13]. In comparison to TiO<sub>2</sub> nanoparticles, studies  
63 have reported improved H<sub>2</sub> production from ethanol under UV light conditions when employing  
64 1D TiO<sub>2</sub> [10, 13]. Hydrothermal synthesis factors such as reaction temperature and the TiO<sub>2</sub>-to-  
65 NaOH molar ratio can significantly affect the 1D TiO<sub>2</sub> phase structure, crystal size, SSA [2, 3, 6,  
66 14] and, subsequently the H<sub>2</sub> production rate. However, the impact of hydrothermal synthesis  
67 factors on the 1D TiO<sub>2</sub> photocatalytic H<sub>2</sub> production rate and optimization of the hydrothermal  
68 conditions have not been addressed in previous studies.

69 Photocatalytic production of H<sub>2</sub> and other fuels is affected by phase structure, crystal size,  
70 BET SSA, bandgap [15-17], band edge positions [17, 18], charge transfer [19], material stability  
71 [20, 21], cocatalyst [22-25], availability [26], complementary metal oxide semiconductor [27, 28]  
72 and toxicity [26]. Substrates such as water [19, 29] and ethanol [24] have been used to produce  
73 H<sub>2</sub> using photocatalysts. Other electron donors (ED) employed to produce H<sub>2</sub> utilizing TiO<sub>2</sub>  
74 under UV light conditions include methanol, 1,2,3 propanetriol and glucose [30].

75 After absorbing photons, photocatalysts generates and separates electrons ( $e^-$ ) and holes ( $h^+$ ).  
76 Next, the photogenerated electrons reduce  $H^+$  to generate  $H_2$ . The water splitting reaction is  
77 described in the following half-cell reactions:



80 In the presence of sacrificial ED [30, 31] such as ethanol, the photogenerated holes react with  
81 the ED and subsequently, the recombination of electrons and holes in photocatalyst are  
82 suppressed [30, 31]. This suppression process significantly increases the  $H_2$  production rate as  
83 well as photocatalytic stability [30, 31]. The photoanode water splitting half reaction is as  
84 follows [24, 32]:



86 Ethanol, a renewable fuel produced mainly from corn, with a specific heating value of  
87 approximately  $29.7 \text{ MJ}\cdot\text{kg}^{-1}$  is less when compared to  $H_2$  with a specific heating value of  
88 approximately  $141.8 \text{ MJ}\cdot\text{kg}^{-1}$  [33]. In addition, the decomposition of ethanol contributes to a  
89 high  $H_2$  production rate and quantum efficiency [34]. Hence,  $H_2$  with a larger energy content is  
90 preferred when compared to ethanol as a fuel source.

91 The first objective of this study was to employ an alkaline hydrothermal method to  
92 synthesize 1D  $TiO_2$  photocatalysts under variable reaction conditions. The second objective was  
93 to employ a three-factor and three-level Box Behnken design (BBD) to evaluate the effects of  
94 selected hydrothermal process conditions (reaction temperature, the NaOH concentration and the  
95  $TiO_2$  precursor concentration) on the photocatalytic 1D  $TiO_2$   $H_2$  production rate. The third  
96 objective was to optimize the hydrothermal conditions and synthesize 1D  $TiO_2$  with a maximum  
97  $H_2$  production rate using the BBD model. The final objective was to decorate the optimized BBD

98 TiO<sub>2</sub> catalyst with Pt and Au noble metals and investigate the photocatalytic H<sub>2</sub> production using  
99 ethanol, methanol, formic acid and 1,2,3 propanetriol.

100

## 101 2. Experimental

102 Commercial TiO<sub>2</sub> nanoparticles (P25) were purchased from Degussa (Evonik Industries,  
103 Germany). NaOH (97% purity), ethanol (95% purity), H<sub>2</sub>AuCl<sub>4</sub> (99.9% purity), (99.5% purity),  
104 methanol (99.8% purity), formic acid (95% purity), 1,2,3 propanetriol (99.5% purity), F-doped  
105 SnO<sub>2</sub>-coated (FTO) glass, polyethylene glycol (PEG, molecular weight 20 000) and HCl (37  
106 wt%) were purchased from Fischer Scientific (Ontario, Canada).

### 107 2.1. Preparation of 1D nanometric TiO<sub>2</sub> photocatalyst

108 1D TiO<sub>2</sub> samples were prepared using the alkaline hydrothermal route [10, 12]. Briefly, TiO<sub>2</sub>  
109 nanoparticles (Aeroxide TiO<sub>2</sub> P25, Evonik Corporation, Parsippany, New Jersey) were added  
110 into 70 mL of a NaOH solution. The TiO<sub>2</sub> concentration and the NaOH concentration used in  
111 the study are shown in Table 1. The mixture (total volume 70 mL) was poured into a 100-mL  
112 Teflon® capped container. The Teflon® container was placed into a stainless-steel bomb, capped  
113 then heated at desired temperature for 48 h and subsequently, cooled to room temperature. The  
114 resulting product was centrifuged and washed with 0.1 M HCl solution. The white paste was  
115 repeatedly washed with deionized water until pH = 7 and calcined at 400°C for 2 h to produce  
116 1D TiO<sub>2</sub> nanomaterials. The hydrothermal conditions for temperature, NaOH concentration and  
117 TiO<sub>2</sub> concentration (Table 1) were based on previous research [14].

118

119

120

Table 1: Three selected factors and three level.

Level	Factors		
	Temperature (°C)	NaOH concentration (M)	TiO <sub>2</sub> concentration (g·L <sup>-1</sup> )
-1	120	5	14
0	150	10	43
1	190	15	100

Note: the reaction mixture volume is 70 mL.

121  
122

## 123 2.2. Characterization studies

124 The 1D TiO<sub>2</sub> photocatalyst morphology was characterized using field emission scanning  
 125 electron microscopy (FESEM; JEOL, Japan) and high resolution transmission electron  
 126 microscopy (HRTEM) (300kV, JEOL 3010, Japan). X-ray diffraction (XRD) analysis of the  
 127 samples was performed using an X-ray diffractometer (Rigaku, MI) equipped with Cu K<sub>α</sub>  
 128 radiation source. An Alpha300 RA argon laser Raman spectrometer (WITec, Germany) with an  
 129 excitation wavelength set at 532 nm was used to conduct the Raman studies. UV-Vis spectra  
 130 analysis was recorded on a Cary 300 UV-Vis (Agilent Technologies, Santa Clara, CA). A  
 131 Micromeritics ASAP 2020 Brunauer–Emmett–Teller (BET) analyzer (Micromeritics Instrument,  
 132 Norcross, GA) was used to obtain nitrogen adsorption–desorption isotherms at 77K. The BET  
 133 SSA for each sample is provided in Table 2.

134  
135  
136  
137  
138  
139  
140

Table 2: Design matrix for experimental factors and response (H<sub>2</sub> production rate, mean crystal size and BET SSA) at different factor levels.

Expt. #	Factors <sup>a</sup>			Response		
	T (°C) (X <sub>1</sub> )	NaOH (M) (X <sub>2</sub> )	TiO <sub>2</sub> (g·L <sup>-1</sup> ) (X <sub>3</sub> )	H <sub>2</sub> production rate (μmol·h <sup>-1</sup> )	Mean crystal size L (nm)	BET SSA (m <sup>2</sup> ·g <sup>-1</sup> )
1	120	5	43	193±7	9.5±0.1	182 ± 5
2	190	5	43	298±10	21.5±0.2	125 ± 5
3	120	15	43	463±14	19.9±0.1	138 ± 3
4	190	15	43	72±4	57.2±0.4	37 ± 3
5	120	10	14	271±8	18.2±0.1	146 ± 5
6	190	10	14	95±4	46.4±0.3	73 ± 3
7	120	10	100	224±8	17.6±0.2	149 ± 5
8	190	10	100	103±5	48.2±0.3	39 ± 3
9	150	5	14	204±8	16.9±0.2	174 ± 5
10	150	15	14	284±10	58.3±0.3	61 ± 3
11	150	5	100	395±13	21.2±0.2	140 ± 4
12	150	15	100	283±10	18.8±0.2	137 ± 5
13	150	10	43	393±13	19.5±0.2	151 ± 4
14	150	10	43	389±12	19.8±0.2	152 ± 5
15	150	10	43	383±8	20.5±0.2	148± 5

Note: <sup>a</sup> T, NaOH and TiO<sub>2</sub> represent temperature, NaOH and TiO<sub>2</sub> concentration. <sup>b</sup> the reaction mixture volume is 70 mL.

141

142 **2.3. Photocatalytic hydrogen production**

143 Photocatalytic experiments were conducted using quartz tubes (25 mm ID × 250 mm length)

144 (Technical Glass Products Inc., Painesville, OH) sealed with aluminum crimp caps and Teflon®

145 lined rubber septa. All reaction conditions were examined in triplicate conditions. The sealed

146 photocatalytic reaction tubes were irradiated with a 300-nm UV light source (LZC-UVB-016

147 lamp, Luzchem, ON, Canada) as described in a previous study by Ray *et al.* [35]. The average

148 intensity of UV irradiance was 9 mW·cm<sup>-2</sup>. The reaction mixture was stirred to maintain the

149 photocatalyst in suspension, minimize particle agglomeration and mass transfer limitation. The

150 reactor temperature was maintained at 37±2°C.



151 The 50-mL reaction mixture contains 0.2 g·L<sup>-1</sup> of the photocatalyst and 20% (v/v) ethanol as  
 152 ED. The reaction mixture was purged with nitrogen (N<sub>2</sub>) gas to remove oxygen. Next, the  
 153 reaction mixture was ultrasonicated and magnetically stirred under dark condition for 1 h before  
 154 initiation with UV light. Next, the reaction mixture was exposed to UV light and maintained at  
 155 37±2°C. At specific time intervals, headspace samples were collected and the H<sub>2</sub> concentration  
 156 was determined using a gas chromatograph (GC) (Varian CP-3800). The GC was configured  
 157 with a 2 m long x 2 mm I.D. Carbon Shin Column (Alltech, Deerfield, IL) and a thermal  
 158 conductivity detector (TCD) at 200°C. The oven and injector temperatures were set at 200°C and  
 159 150°C, respectively. Nitrogen gas was used as a carrier gas at a flowrate of 15 mL·min<sup>-1</sup>. The  
 160 GC detection limit was approximately 310 μmol·L<sup>-1</sup> for H<sub>2</sub>. The photocatalyst reaction mixture  
 161 was irradiated for 5 h using a 300-nm monochromatic UV light source. The irradiation area for  
 162 reaction mixture in each tube was 58 cm<sup>2</sup>. The H<sub>2</sub> production rate (μmol·h<sup>-1</sup>) for each sample is  
 163 shown in Table 2.

164 The quantum efficiency (ε) was calculated using Eq. (4) and (5) [36].

$$165 \quad N = \frac{E\lambda}{hc} = \frac{9 \times 10^{-3} \times 58 \times 3600 \times 300 \times 10^{-9}}{6.626 \times 10^{-34} \times 3 \times 10^8} = 2.83 \times 10^{21} \quad (4)$$

$$167 \quad \varepsilon = \frac{2 \times \text{the number of evolved hydrogen molecules}}{\text{the number of incident photons}} \times 100\% \\
 168 \quad = \frac{2 \times 6.02 \times 10^{23} \times H_2 \text{ production rate} \times 1h}{2.83 \times 10^{21}} \times 100\% \quad (5)$$

170 Where N is the photon number in 1 h; E is the energy rate of incident photons; λ is the  
 171 wavelength in nm; h is Planck's constant; and c is the photon velocity. Additional photocatalytic  
 172 H<sub>2</sub> production experiments were conducted using solar irradiation (310-800 nm) (LZC-VIS-016,  
 173

174 Luzchem, ON, Canada) with average intensity of 2 mW·cm<sup>-2</sup>. Other EDs examined in the study  
175 included 20% (v/v) methanol, 20% (v/v) formic acid and 20% (v/v) 1,2,3 propanetriol.

176

177

#### 178 2.4. Optimization study

179 The experimental design was based on a 3-factor and 3-level Box-Behnken design (BBD)  
180 [37]. The experimental design was used to optimize key process factors (Table 1) to improve the  
181 H<sub>2</sub> production rate with using ethanol as the ED. A total of 15 experimental points (#1 to #15)  
182 were conducted with each condition under triplicate (Table 2). Experiments, designated as #13,  
183 #14 and #15, were conducted as central points to evaluate the magnitude of the error in the study.  
184 The experimental factors and H<sub>2</sub> production rate (Y) (response variable) were modeled using  
185 Minitab 15 (Minitab Inc., State College, PA) to fit a full quadratic equation (Eq. (6)):

186

$$187 \quad Y = a_0 + \sum_{i=1}^3 a_i X_i + \sum_{i=1}^3 a_{ii} X_i^2 + \sum_{i=1}^3 \sum_{i<j=2}^3 a_{ij} X_i X_j \quad (6)$$

188

189 where X<sub>i</sub>'s are input variables which influence the response variable Y, a<sub>0</sub> is an offset term, a<sub>i</sub> is  
190 the i<sup>th</sup> linear coefficient, a<sub>ii</sub> is the quadratic coefficient, and a<sub>ij</sub> is the ij<sup>th</sup> interaction coefficient.  
191 The X<sub>1</sub>, X<sub>2</sub> and X<sub>3</sub> represent the synthesis temperature, NaOH concentration and TiO<sub>2</sub>  
192 concentration, respectively (Table 2).

193 The quadratic model was employed to predict reaction conditions which produced 1D TiO<sub>2</sub>  
194 with a maximum H<sub>2</sub> production rate. A D-optimality analysis [38] was performed to find  
195 optimal conditions for the three factors under consideration (maximize the H<sub>2</sub> production rate).  
196 The coefficient values for fitting the full quadratic model were determined using the H<sub>2</sub>  
197 production rate and a multiple regression analysis. An analysis of variance (ANOVA) was

198 conducted using the observed responses for samples #1 to #15) (Table 2). Only significant terms  
199 with p values < 0.05 were included into the model. A normal distribution plot together with the  
200 Anderson-Darling (AD) [35] test was used to determine the adequacy of the model.

201

## 202 **2.5. *TiO<sub>2</sub> photocatalyst decorated with Au and Pt nanoparticles***

203 The TiO<sub>2</sub> photocatalyst sample was decorated with Au nanoparticles based on work by Pu et  
204 al. [39]. 1D TiO<sub>2</sub> (500 mg of optimized 1D TiO<sub>2</sub> synthesized at 126°C, 15 M NaOH and 49 g·L<sup>-1</sup>  
205 TiO<sub>2</sub>) was first dispersed in the reaction mixture consisting of 500 mL deionized water and 250  
206 mL ethanol followed by the addition of 10 mL of 0.1 M NaOH solution. The mixture was heated  
207 to 50°C, followed by addition of 6 mL of a 5 mM HAuCl<sub>4</sub> solution. Ethanol was used as a  
208 reducing agent to facilitate Au growth. The mixed solution was maintained at 50°C for 3 h with  
209 vigorous stirring. The product (Au-decorated 1D TiO<sub>2</sub> with the Au content of 2 wt%) was  
210 filtered, washed with deionized water and ethanol, and then dried at 60°C in air for 12 h. For the  
211 Pt-decorated 1D TiO<sub>2</sub> with a Pt content of 2 wt%, a similar procedure was employed with using  
212 H<sub>2</sub>PtCl<sub>6</sub> as Pt source and UV light was used to assist in the reduction of H<sub>2</sub>PtCl<sub>6</sub> to Pt.

213

## 214 **3. Results and discussion**

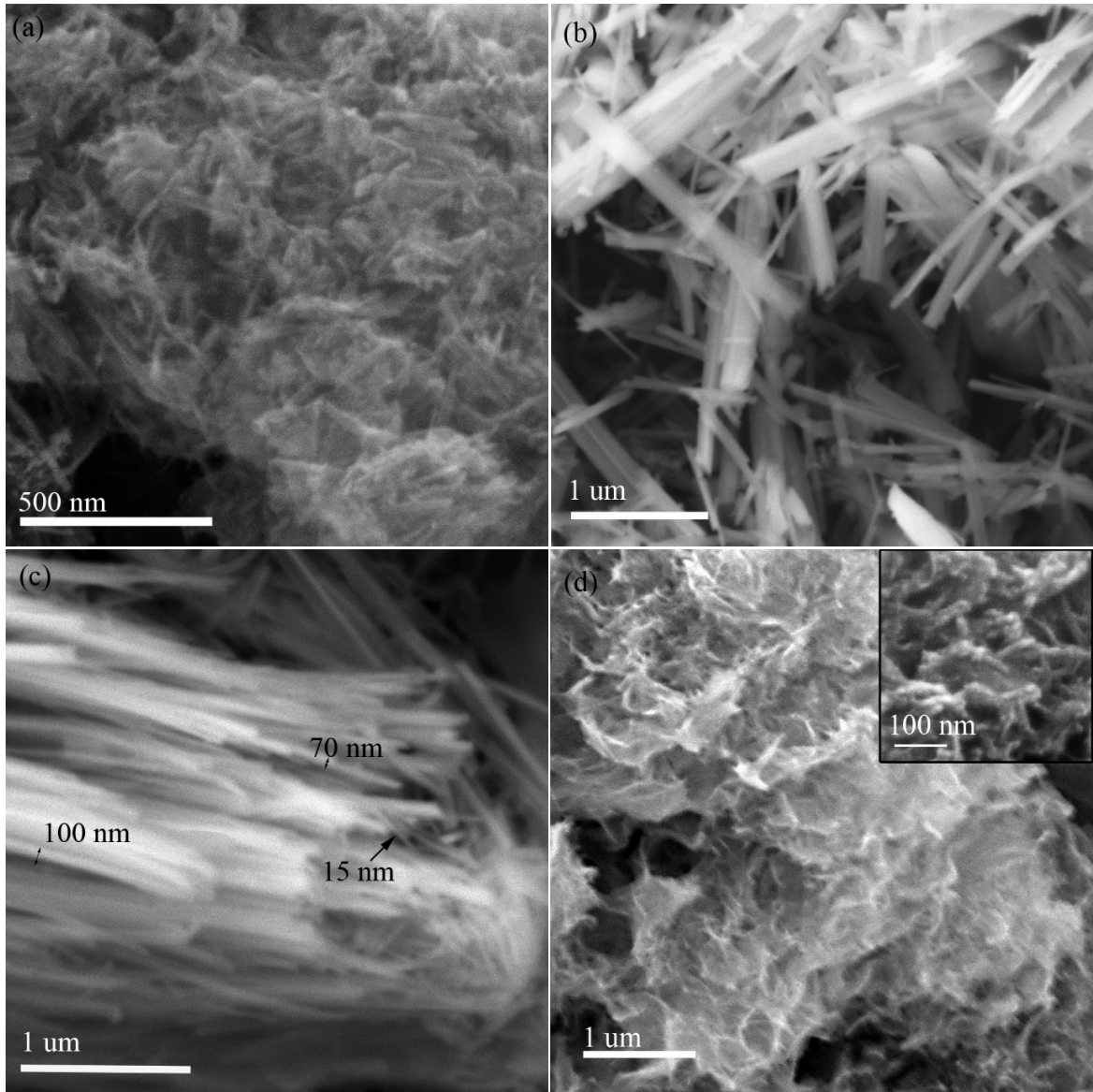
### 215 *3.1. 1D TiO<sub>2</sub> morphology*

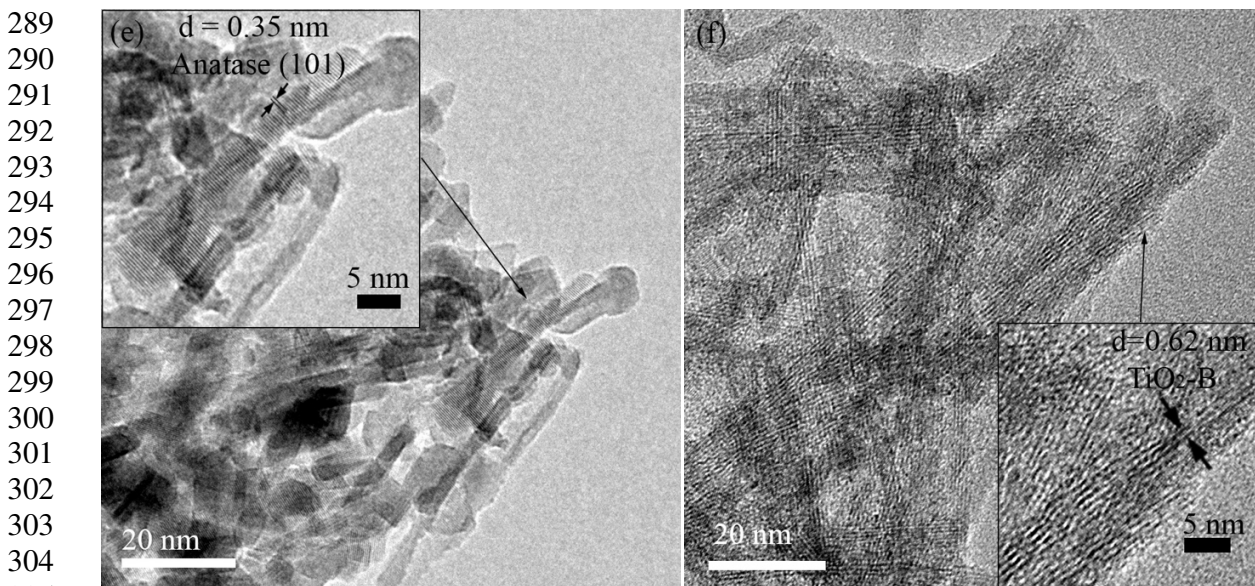
216 Field emission scanning electron microscopy (FESEM) and high resolution transmission  
217 electron microscopy (HRTEM) images for selected 1D TiO<sub>2</sub> samples are shown in Figure 1. 1D  
218 structures (nanorods and nanowires) with large differences in the diameter and length were  
219 characteristic of TiO<sub>2</sub> synthesized under different reaction conditions. Nanorods morphology  
220 with lengths ranging from 20 nm to 100 nm and the diameter of approximately 10 nm were

221 **observed in the sample** (#1) (Figure 1a) synthesized at 120°C and with 5 M NaOH plus 43 g·L<sup>-1</sup>  
222 TiO<sub>2</sub> (Figure 1e). Lattice fringes observed with 0.35 nm spacing (Figure 1e) indicate the  
223 presence of anatase in the 1D TiO<sub>2</sub> structure (sample #1) [40]. Increasing reaction temperatures  
224 and NaOH concentrations caused increasing length, increasing diameter and phase structure  
225 changes. Nanowire morphology with lengths reaching 3 μm and diameter ranging from 10 nm to  
226 100 nm was observed for **sample #4 (synthesized at 190°C, 15 M and 43 g·L<sup>-1</sup>)** (Figure 1b). The  
227 FESEM image for sample #8 (190°C, 10 M and 100 g L<sup>-1</sup>) (Figure 1c) indicates nanowires with  
228 lengths in the micrometer range. The wide distribution of diameter for sample #8 was variable  
229 from 10 nm to hundreds of nanometers. The lattice fringes of with 0.62 nm spacing (Figure 1f)  
230 indicate the TiO<sub>2</sub> nanowire (sample #8) consisted of the TiO<sub>2</sub>-B phase [41]. The FESEM image  
231 for sample #9 (**150°C, 5 M and 14 g L<sup>-1</sup>**) (Figure 1d) indicate nanowires with lengths in the  
232 hundreds of nanometers range. Lowering the temperature as well as lower NaOH concentration  
233 levels were linked to smaller diameter and decreasing crystal size (sample #1). In comparison,  
234 higher temperatures and NaOH concentrations were associated with larger diameter (Sample # 6  
235 and 8), increasing length (sample #9) and increasing crystal size. The FESEM images provided  
236 evidence showing the hydrothermal synthesis factors significantly impacted the 1D TiO<sub>2</sub>  
237 diameter and crystal size. **The formation of 1D TiO<sub>2</sub> nanostructures was controlled by shearing,**  
238 **exfoliation, delamination of lamellar nanosheets and scrolling lamellar nanosheets into 1D**  
239 **structure [42, 43].**

240  
241  
242  
243

244  
245  
246  
247  
248  
249  
250  
251  
252  
253  
254  
255  
256  
257  
258  
259  
260  
261  
262  
263  
264  
265  
266  
267  
268  
269  
270  
271  
272  
273  
274  
275  
276  
277  
278  
279  
280  
281  
282  
283  
284  
285  
286  
287  
288





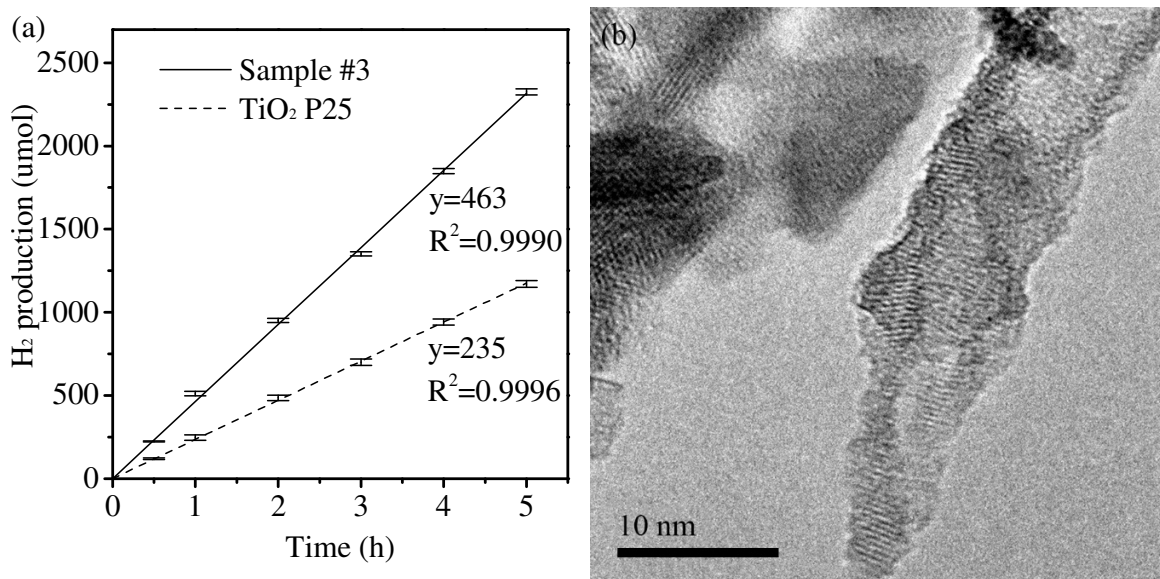
306 Figure 1: 1D TiO<sub>2</sub> field emission scanning electron microscopy (FESEM) and high resolution  
307 transmission electron microscopy (HRTEM) images (a) FESEM image for sample #1  
308 synthesized at 120°C, 5 M NaOH and 43 g·L<sup>-1</sup>; (b) FESEM image for sample #4 synthesized at  
309 190°C, 15 M NaOH and 43 g·L<sup>-1</sup>; (c) FESEM image for sample #8 synthesized at 190°C, 10 M  
310 and 100 g·L<sup>-1</sup>; (d). FESEM image for sample #9 synthesized at 150°C, 5 M NaOH and 14 g·L<sup>-1</sup>;  
311 (e) HRTEM image sample #1 synthesized at 120°C, 5 M NaOH and 43 g·L<sup>-1</sup> and (f) HRTEM  
312 image for sample #8 synthesized at 190°C, 10 M and 100 g·L<sup>-1</sup>.

313

### 314 3.2. Photocatalytic hydrogen production

315 Significant differences in H<sub>2</sub> production were observed for 1D TiO<sub>2</sub> samples prepared using  
316 different reaction conditions. Hydrogen production versus time profiles are shown in Figure 2a  
317 for BBD sample #3 plus the P25 control. Control experiments were conducted employing with  
318 and without P25 nanoparticles. The mean H<sub>2</sub> production rate (Y value) was 0 μmol·h<sup>-1</sup> without a  
319 photocatalyst; however, with the addition of P25 nanoparticles, the mean production rate  
320 increased to 235±8 μmol·h<sup>-1</sup>. In comparison, the production rate of 463±14 μmol·h<sup>-1</sup> (ε =  
321 19.3 ± 0.6%) for sample #3 (synthesized at 120°C, 15 M NaOH and 43 g·L<sup>-1</sup> TiO<sub>2</sub>) was  
322 approximately 2-fold larger than P25 (ε = 10.0 ± 0.4%) using ethanol as an ED. **Notice sample**  
323 **#3 was characteristic with nanorods structure of approximately 10 nm diameter (Figure 2b).** The

324  $\epsilon$  value for the Pt-TiO<sub>2</sub> catalyst was 5-fold greater than the  $\epsilon$  value for TiO<sub>2</sub> when employing  
325 pure water as a substrate under UV light conditions . The photocatalytic H<sub>2</sub> production rate  
326 showed an approximate 110-fold increase using 20 v/v% ethanol as an ED when compared to  
327 using water (Figure S1). The H<sub>2</sub> production rates are listed in Table 2. The effect of ethanol  
328 concentration on H<sub>2</sub> production rate was evaluated (Figure S1). For various ethanol  
329 concentrations tested, the highest H<sub>2</sub> production rate was observed when using a 20 v/v%  
330 aqueous ethanol solution.



331 Figure 2: (a) H<sub>2</sub> production (b) High resolution transmission electron microscopy (HRTEM)  
332 image for sample #3 and TiO<sub>2</sub> precursor using 300-nm UV light.  
333  
334

### 335 3.3. Modeling and effects of factors on the H<sub>2</sub> production rate (response variable) for ethanol

336 For the response surface optimization study, three sets (replicates) of 15 experiments were  
337 conducted to compute the H<sub>2</sub> production rate under 15 conditions (Table 2). A multiple  
338 regression analysis was used to develop a full quadratic equation (7) which describes the H<sub>2</sub>  
339 production rate, Y, as a function of the hydrothermal process conditions.

340

341  $Y = -2964 + 34.28X_1 + 124.34X_2 + 8.55X_3 - 0.7X_1X_2 + 0.006X_1X_3 - 0.239X_2X_3 -$   
342  $0.096X_1^2 - 0.269X_2^2 - 0.058X_3^2$  (7)

343

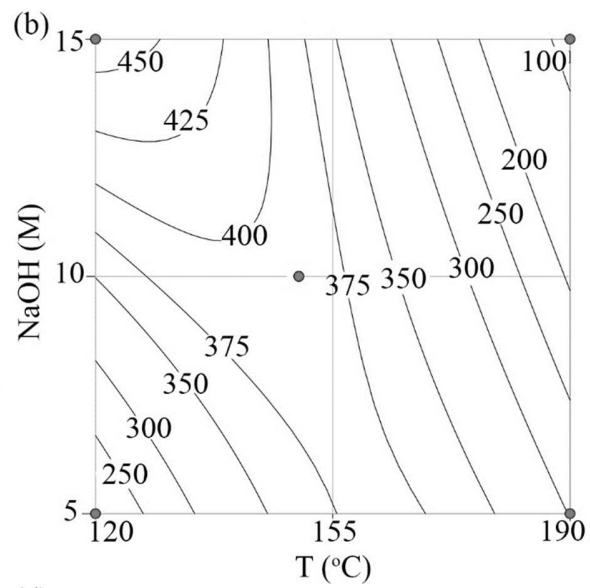
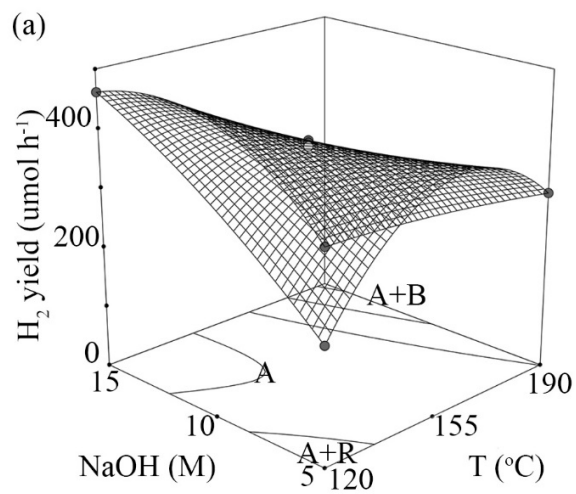
344 where Y is the H<sub>2</sub> production rate (μmol·h<sup>-1</sup>), X<sub>1</sub>, X<sub>2</sub> and X<sub>3</sub> represent the reaction temperature  
345 (°C), NaOH concentration (M) and TiO<sub>2</sub> concentration (g·L<sup>-1</sup>), respectively.

346 The relationship between the synthesis factors, phase structure and the H<sub>2</sub> production rate is  
347 shown in the 3D surface plots and the corresponding contour plots (Figure 3). Interaction  
348 between the temperature and the NaOH concentration (Figures 3a and b) suggests that both  
349 parameters significantly affected the 1D TiO<sub>2</sub> phase structure and the H<sub>2</sub> production rate (Figure  
350 S2). A relatively low temperature at 120°C and a high NaOH concentration at 15 M were closely  
351 associated with producing a pure anatase catalyst with a high H<sub>2</sub> production rate. Increasing  
352 temperatures or decreasing NaOH concentrations were correlated with decreasing H<sub>2</sub> production  
353 rates. The biphasic anatase-rutile structure, synthesized at 120°C and 5 M NaOH, was linked to a  
354 lower H<sub>2</sub> production rate. In addition, a significant decrease in the H<sub>2</sub> production rate was  
355 observed for the biphasic anatase-TiO<sub>2</sub>-B structure which was synthesized at 190°C and with ≥10  
356 M NaOH. These observations indicate the rutile and TiO<sub>2</sub>-B phases are closely correlated with  
357 decreasing photocatalytic H<sub>2</sub> production. Interaction between temperature and TiO<sub>2</sub>  
358 concentration (Figure 3c and d) and interaction between NaOH concentration and TiO<sub>2</sub>  
359 concentration (Figure 3e and f) confirmed decreasing the synthesis temperature and increasing  
360 the NaOH concentration were closely associated with increasing the H<sub>2</sub> production rate. In  
361 addition, the surface and contour plots indicate the optimum H<sub>2</sub> production rate was obtained  
362 with a TiO<sub>2</sub> concentration of approximately 50 g·L<sup>-1</sup>.

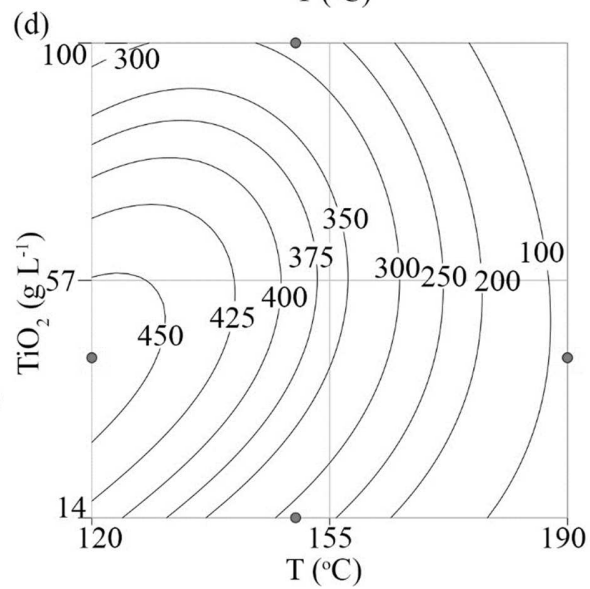
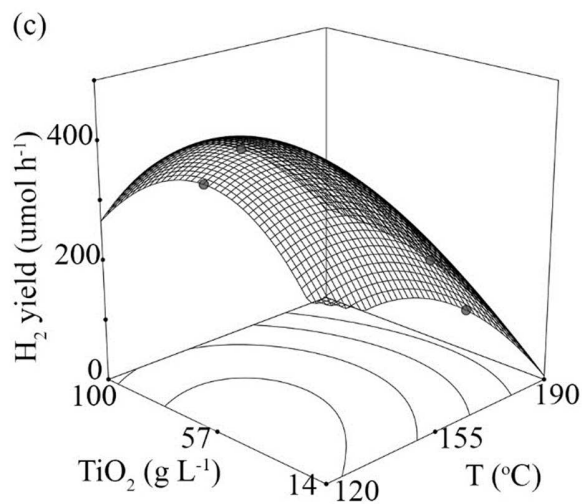
363



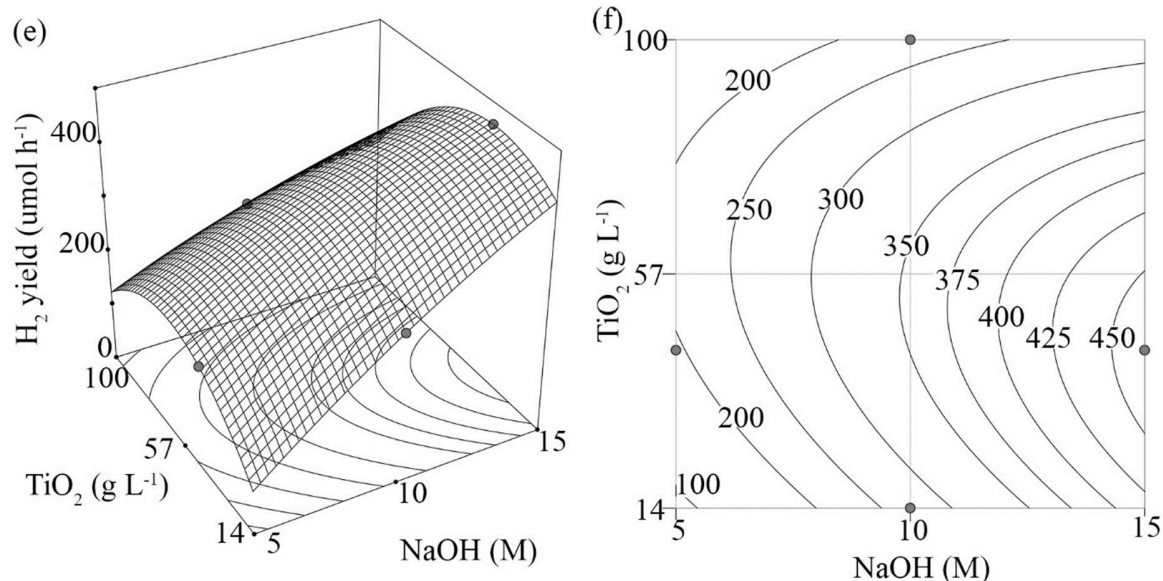
364 The D-optimality index was used to locate the maximum response (Y) region within the  
365 factor space under consideration (Figure S3). A maximum response of  $470 \mu\text{mol}\cdot\text{h}^{-1}$  was  
366 predicted for 1D  $\text{TiO}_2$  synthesized at  $126^\circ\text{C}$ , 15 M NaOH and  $49 \text{ g}\cdot\text{L}^{-1}$   $\text{TiO}_2$ . Additional  
367 experiments were conducted to verify the maximum response when using the 1D  $\text{TiO}_2$   
368 photocatalyst under the predicted conditions. The predicted value was slightly underestimated  
369 when compared to the observed response of  $475\pm 12 \mu\text{mol}\cdot\text{h}^{-1}$  ( $\epsilon=20.2\pm 0.5\%$ ). Recall, pure  
370 anatase with a mean crystal size of  $20.1\pm 0.2 \text{ nm}$  and BET SSA of  $140\pm 3 \text{ m}^2\cdot\text{g}^{-1}$  was observed for  
371 1D  $\text{TiO}_2$  synthesized under optimum conditions. The optimum  $\text{H}_2$  production rate value was  
372 approximately 2-fold larger when compared to commercial P25 when employing a 20 v/v%  
373 ethanol feed. This  $\text{H}_2$  production rate was significantly improved when compared to reported  
374 production rates of  $348 \mu\text{mol}\cdot\text{h}^{-1}$  for biphasic anatase- $\text{TiO}_2$ -B [10]. **The optimum  $\text{H}_2$  production**  
375 **rate of  $470 \mu\text{mol}\cdot\text{h}^{-1}$  for the optimized 1D  $\text{TiO}_2$  was normalized to a mass basis. The specific  $\text{H}_2$**   
376 **production rate (per g of photocatalyst) attained was  $23,500 \mu\text{mol}\cdot\text{h}^{-1}\cdot\text{g}^{-1}$ .** The maximum specific  
377  $\text{H}_2$  production rate was significantly enhanced when compared to data reported for pure anatase,  
378 pure rutile, flame spray pyrolysis-synthesised  $\text{TiO}_2$  and Au/ $\text{TiO}_2$  [44].  
379



380



381



382  
 383  
 384 Figure 3: 3D response surface and contour plots for: (a) and (b) Interaction between  
 385 hydrothermal temperature and NaOH concentration set at 43 g·L<sup>-1</sup> TiO<sub>2</sub>, (c) and (d) Interaction  
 386 between hydrothermal temperature and TiO<sub>2</sub> concentration set at 15 M NaOH concentration, (e)  
 387 and (f) Interaction between NaOH concentration and TiO<sub>2</sub> concentration set at 120°C  
 388 temperature.

389 Note: A, R and B represents the anatase, rutile and TiO<sub>2</sub>-B phases, respectively.

390

### 391 3.4. Response surface model development

392 An analysis of variance (ANOVA) (Table S1) of the model full quadratic equation (7) was  
 393 employed to determine the significance and adequacy of the model. The quadratic model with an  
 394 overall p-value ≤ 0.05 [37, 38, 45, 46] and a F-value ≤ to the critical value (2.01 at 5% level of  
 395 significance) [37, 38, 45, 46] indicate the model was statistically significant. However, two  
 396 variables ( $X_2^2$  and  $X_1X_3$ ) with p-value ≥ 0.05 were statistically insignificant with no individual  
 397 effect on the full quadratic model. These terms were deleted from model using a backward  
 398 elimination method [38]. The revised response surface model is designated as equation (8):

399

$$400 Y = -2974 + 34.43X_1 + 118.96X_2 + 9.40X_3 - 0.7X_1X_2 - 0.239X_2X_3 - 0.095X_1^2 - 0.058X_3^2$$

401 (8)

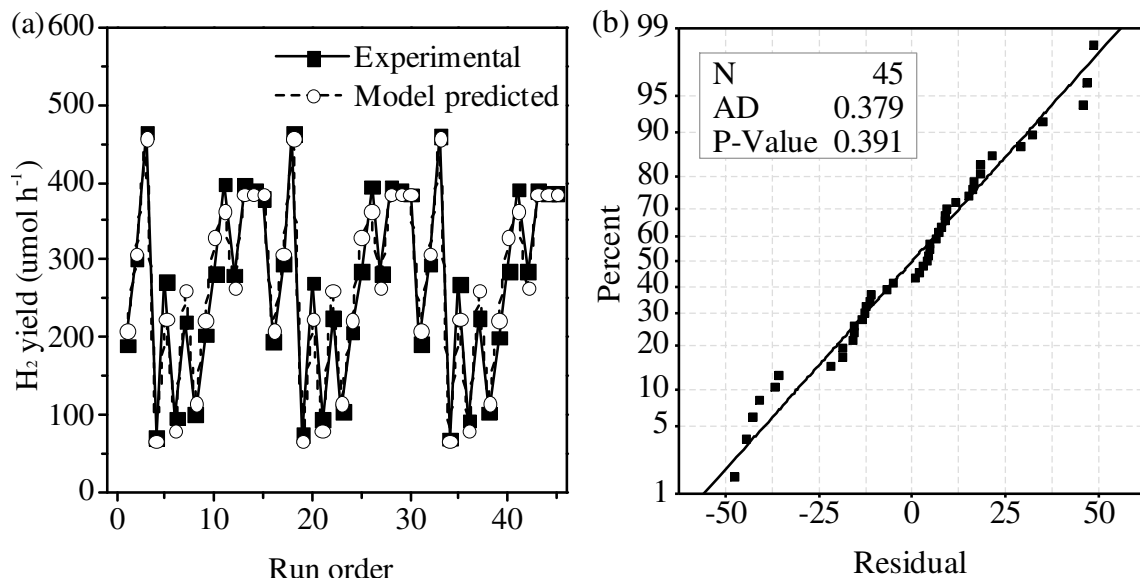
402

403 where Y is the H<sub>2</sub> production rate ( $\mu\text{mol}\cdot\text{h}^{-1}$ ), X<sub>1</sub>, X<sub>2</sub> and X<sub>3</sub> represent temperature ( $^{\circ}\text{C}$ ), NaOH  
404 concentration (M) and TiO<sub>2</sub> concentration ( $\text{g}\cdot\text{L}^{-1}$ ), respectively.

405

### 406 3.5. Response surface model verification

407 A scatter plot comparing the experimental and the model predicted values (Figure 4a)  
408 indicate a reasonable correlation at each level. The Anderson-Darling (AD) statistic (Figure 4b)  
409 was employed to assess the adequacy of fitting the model to the experimental data by  
410 determining the normal distribution of the residuals (difference between the predicted and  
411 experimental values) [47]. An AD value of 0.379 ( $\leq$  the critical value of 0.735 for 45 samples  
412 and at a 5% level of significance) [47] and a p-value of 0.391 ( $\geq$  0.05) suggest the model's  
413 predicted values correlated with the experimental values.



414

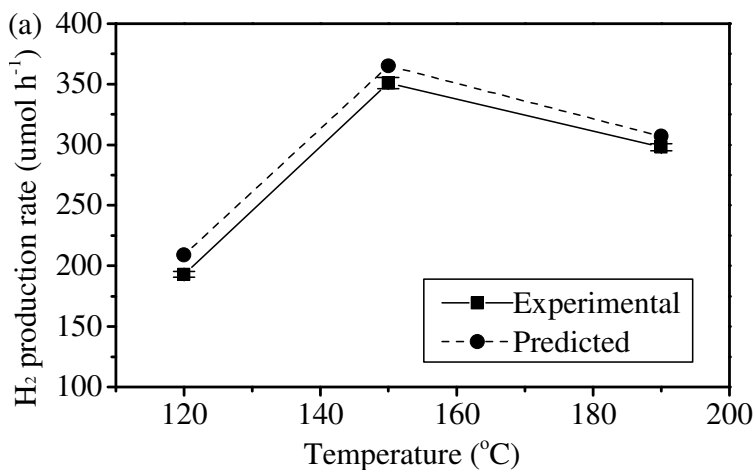
415 Figure 4: Accuracy evaluation of the response surface model. (a) Scatter plot of the H<sub>2</sub>  
416 production rate ( $\mu\text{mol}\cdot\text{h}^{-1}$ ) versus experiment order (45 experiments). (b) Anderson-Darling  
417 normality plot of residuals.

418 Notes: N = the number of experiments conducted in this study; P-Value = level of confidence;  
419 AD = Anderson-Darling statistic.

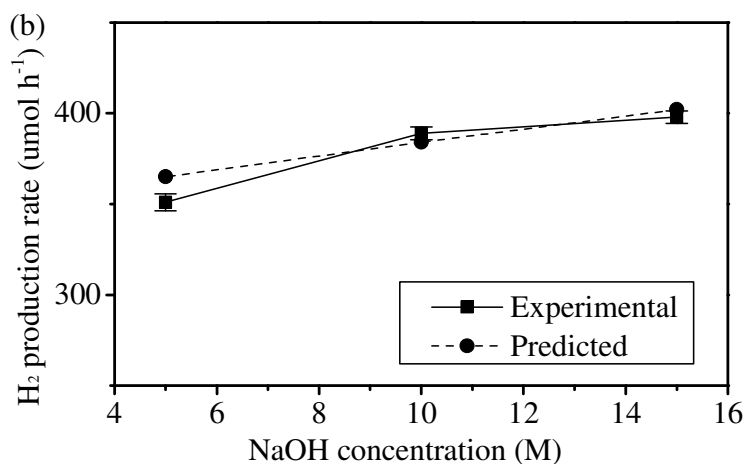
420

421 Validation of the model accuracy was examined by varying a single factor in three additional  
422 experiments (Figure 5). The model predicted trend was comparable to the experimental trend for  
423 varying each factor. For a temperature range from 120 to 190°C (Figure 5a), the model predicted  
424 values were close to the experimental values with a slight overestimate at each temperature level.  
425 For the NaOH concentration (Figure 5b), the predicted values were in agreement with the  
426 experimental data with a slight overestimate at 5 M NaOH. For the TiO<sub>2</sub> concentration, the  
427 model predicted values which were reasonably close to the observed values for each level of  
428 TiO<sub>2</sub> concentration with a slight underestimate at 100 g·L<sup>-1</sup> TiO<sub>2</sub> and a slight overestimate at 14  
429 and 43 g·L<sup>-1</sup> (Figure 5c). **Additional experiments (Table S2) were conducted to compare the**  
430 **model predicted value and experimental value. The results indicate the model's predicted values**  
431 **correlated with the experimental values.**

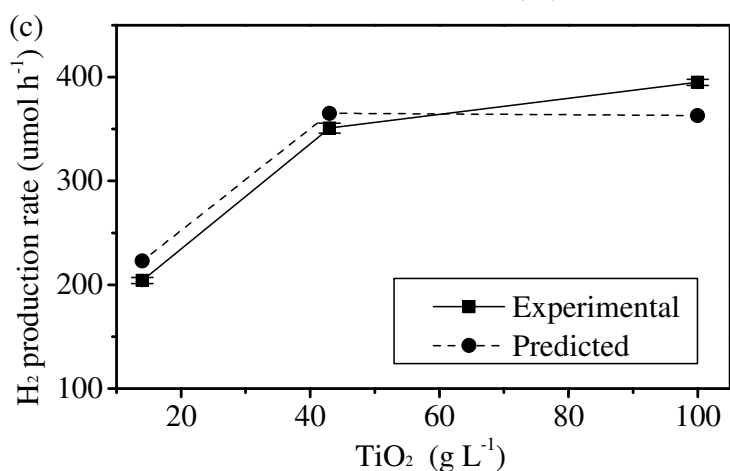
432



433



434



435

436 Figure 5: Validation study of the response surface model for the varied factors under  
 437 consideration. (a) H<sub>2</sub> production rate versus temperature at experimental conditions set at 5 M  
 438 NaOH and 43 g·L<sup>-1</sup> TiO<sub>2</sub>; (b) H<sub>2</sub> production rate value versus NaOH concentration at  
 439 experimental conditions set at 150°C and 43 g·L<sup>-1</sup> TiO<sub>2</sub>; (c) H<sub>2</sub> production rate versus TiO<sub>2</sub>  
 440 concentration at experimental conditions set at 150°C and 5 M NaOH.

441

### 442 3.6. Phase structure, crystal size and bandgap energies

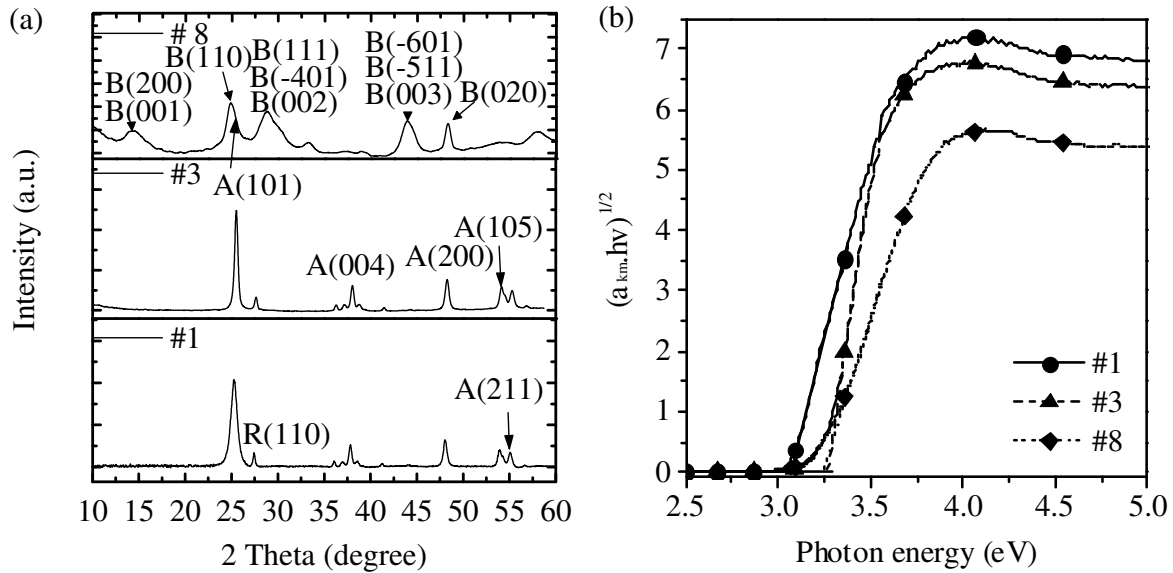
443 XRD analysis and diffuse reflectance UV-Vis spectroscopy were used to evaluate the phase  
 444 structure, crystal size and bandgap energy for the BBD samples. The XRD patterns for selected  
 445 BBD samples #1, #3 and #8 are shown in Figure 6a and the phase structure is summarized in  
 446 Table 3 for all the samples. The three phase structures observed in this study included pure  
 447 anatase [48], biphasic anatase-rutile [49-51] and the biphasic anatase-TiO<sub>2</sub>-B [10] structures  
 448 (Figure 6a). The biphasic anatase-rutile structure, similar to that in P25, was only detected in

449 sample #1 [49-51] (Figure S4), while pure anatase phase and the biphasic anatase-TiO<sub>2</sub>-B  
 450 structures were observed in a majority of the samples. The mean crystal sizes (L, nm) for sample  
 451 #1-15 (Table 2) were calculated using the Scherrer equation (equation 9) and XRD data.

$$452 \quad L = K\lambda / \beta \cdot \cos\theta \quad [52] \quad (9)$$

453 where K,  $\lambda$  and  $\beta$  represent the shape factor (0.89), the wavelength of XRD radiation (0.154 nm)  
 454 and the half maximum of a full peak, respectively.

455



456 Figure 6: X-ray diffraction (XRD) patterns and  $\alpha_{km}h\nu)^{1/2}$  versus absorbed energy for samples #1,  
 457 #3, and #8: (a) XRD spectra and (b)  $\alpha_{km}h\nu)^{1/2}$  versus absorbed energy profiles.

458 Notes: <sup>a</sup>. Synthesis parameter details are listed in Table 2; <sup>b</sup>. A, R and B represents the anatase, rutile and TiO<sub>2</sub>-B phases, respectively.

461

462

463

464

465

466

Table 3. Phase structures, bandgap energies, mean crystal size, BET SSA and H<sub>2</sub> production rate for all BBD samples.

Phase	Sample #	Bandgap energy (eV)	Mean crystal size (nm)	BET SSA (m <sup>2</sup> ·g <sup>-1</sup> )	H <sub>2</sub> production rate (μmol·h <sup>-1</sup> )
Anatase and rutile	1	3.067±0.006	9.5±0.1	182±5	193±7
Anatase	2, 3, 5, 7, 9, 10, 11, 12, 13, 14 and 15	3.258±0.003 to 3.298±0.005	16.9±0.2 to 57.2±0.4	61±3 to 174±5	204±8 to 463±14
Anatase and TiO <sub>2</sub> -B	4, 6, 8	3.210±0.007 to 3.229±0.009	46.4±0.3 to 58.3±0.3	37±3 to 73±3	72±4 to 103±5

Note: Sample order number is defined in Table 2.

468

469 Diffuse reflectance UV-Vis spectroscopic profiles for selected BBD samples are shown in  
 470 Figure S5. All the BBD samples with an optical absorption below 400 nm was likely caused by  
 471 their band-band electron transition [49, 53]. The diffuse reflectance spectra was transformed into  
 472 corresponding absorption spectra (Figure 6b) using Kubelka-Munk function [54]. The bandgap  
 473 energy is closely correlated with the phase structure and chemical composition (Table 3). The  
 474 pure anatase (e.g. sample #3) phase was observed with a large bandgap energy ranging from  
 475 3.258±0.003 to 3.298±0.005 eV [55, 56], while the biphasic structure anatase-rutile (sample #1)  
 476 and anatase-TiO<sub>2</sub>-B (samples #4, #6 and #8) showed decreasing bandgap energies of  
 477 3.067±0.006 and values ranging from 3.210±0.007 to 3.229±0.009 eV, respectively. In the Ti2p  
 478 XPS spectra for sample #1 and the optimized 1D TiO<sub>2</sub> (Figure S6) sample, the two main peaks at  
 479 458.9 eV (Ti2p<sub>3/2</sub>) and 464.5 eV (Ti2p<sub>1/2</sub>) indicate the presence of Ti<sup>4+</sup>. In comparison, the  
 480 deconvoluted peaks located at 457.4 eV (Ti2p<sub>3/2</sub>) and 463.0 eV (Ti2p<sub>1/2</sub>) were due to the presence



481 of  $Ti^{3+}$ . The low peak intensity attributed to  $Ti^{3+}$  indicate sample #1 and the optimized 1D  $TiO_2$   
482 contained a small amount of  $Ti^{3+}$  and oxygen vacancy.

483

### 484 3.7. The effect on phase structure and crystal size

485 The  $H_2$  production rates, crystal size and BET SSA are summarized in Table 3 for the BBD  
486 1D  $TiO_2$  samples synthesized under different reaction conditions. Depending on the  
487 hydrothermal synthesis conditions, the  $H_2$  production rates was variable from  $72\pm 4$  to  $475\pm 12$   
488  $\mu\text{mol}\cdot\text{h}^{-1}$ . The 1D  $TiO_2$  phase structures marked in the 3D response surface plot (Figure 3a)  
489 shows the effect of reaction temperature and NaOH concentration on the phase structure and  $H_2$   
490 production rate. The low NaOH concentration (5 M) and reaction temperature ( $120^\circ\text{C}$ ) were  
491 correlated with the biphasic anatase-rutile structure. Increasing NaOH concentration and  
492 reaction temperature were related to converting rutile into anatase. In addition, higher NaOH  
493 concentrations greater than 10 M coupled with a temperature at  $190^\circ\text{C}$  were associated with the  
494 conversion of anatase to  $TiO_2\text{-B}$ . Variation of the phase structures had a main effect on the  $H_2$   
495 production rate. The pure anatase (sample #2, #3, #5, #7, #9, #11-15 and the optimized sample  
496 synthesized at  $126^\circ\text{C}$ , 15 M NaOH and  $49\text{ g}\cdot\text{L}^{-1}$   $TiO_2$ ) were closely linked with increasing the  $H_2$   
497 production rate, while the biphasic anatase-rutile (sample #1) and anatase- $TiO_2\text{-B}$  structures  
498 (sample #4, #6 and #8) were associated with decreasing  $H_2$  production rate. The pure anatase  
499 samples were correlated with high bandgaps ranging from  $3.258\pm 0.003$  to  $3.298\pm 0.005$  eV.  
500 However, the biphasic anatase-rutile sample #1 showed the lowest bandgap of  $3.067\pm 0.006$  eV.  
501 The lowest  $H_2$  production rate was detected for the biphasic anatase- $TiO_2\text{-B}$  structure (sample #4,  
502 6 and 8). The biphasic anatase- $TiO_2\text{-B}$  samples showed decreased bandgaps ranging from  
503  $3.210\pm 0.007$  to  $3.229\pm 0.009$  eV when compared to the pure anatase samples. The I-t curves for

504 sample #1 (biphasic anatase-rutile), #8 (biphasic anatase-TiO<sub>2</sub>-B), optimized 1D TiO<sub>2</sub> (anatase)  
505 and P25 with an on-off UV-light irradiation (300 nm) source are shown in Figure S7. The  
506 greatest photocurrent density was observed for the optimized 1D TiO<sub>2</sub> containing anatase. This  
507 observation suggests the optimized 1D TiO<sub>2</sub> is characterized by an enhanced charge carrier  
508 transportation and separation. The photocurrent densities for sample #1 and P25 were  
509 comparable to each other. The lowest photocurrent density caused by the fast recombination of  
510 electrons and holes was detected for the sample (#8) containing in the TiO<sub>2</sub>-B phase.

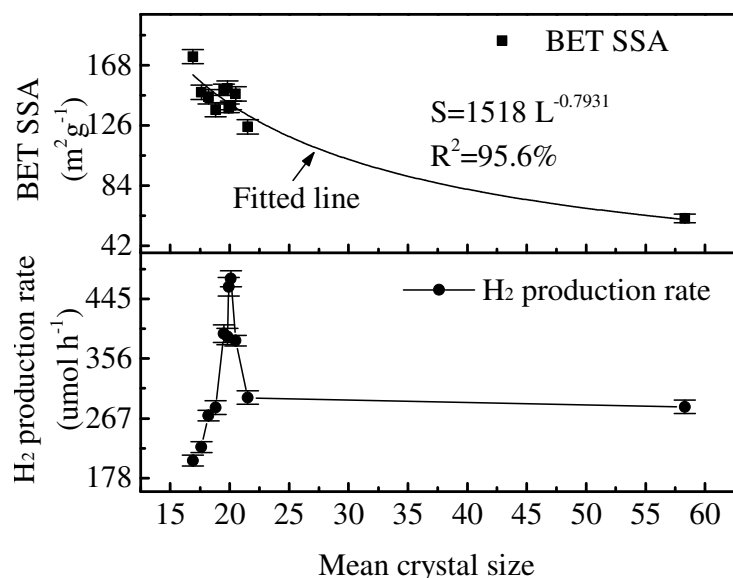
511 The H<sub>2</sub> production rate (μmol·h<sup>-1</sup>) for the pure anatase phase samples (Figure 7) suggests the  
512 greatest H<sub>2</sub> production rate of 475±12 μmol·h<sup>-1</sup> was observed when the mean crystal size was  
513 20.1±0.2 nm with BET SSA of 140±3 m<sup>2</sup>·g<sup>-1</sup>. Smaller crystal size was closely linked to a larger  
514 BET SSA for 1D TiO<sub>2</sub> containing anatase. The BET SSA (m<sup>2</sup>·g<sup>-1</sup>) as a function of the mean  
515 crystal size is shown as equation (Eq. 10).

516

$$517 \quad S = 1518 \times L^{-0.7931} \quad (16 \leq L \leq 56 \text{ and } R^2 = 95.6\%) \quad (10)$$

518

519 Where S (m<sup>2</sup>·g<sup>-1</sup>) and L (nm) represent the BET SSA and the mean crystal size, respectively.



520 Figure 7: Hydrogen production rate and specific surface area versus anatase mean crystal size.  
 521 Note: All samples counted in the figure is anatase phase. The L and S represent crystal size and  
 522 BET SSA, respectively.  $16 \leq L \leq 56$ .  
 523  
 524

525 Increasing the H<sub>2</sub> production rate was closely correlated with decreasing the anatase mean  
 526 crystal size from  $58.3 \pm 0.3$  to  $20.1 \pm 0.2$  nm. The increasing the H<sub>2</sub> production rate was due to  
 527 increasing the SSA [57] and faster rates of e<sup>-</sup> and h<sup>+</sup> surface reactions with the substrate. The  
 528 optimum anatase mean crystal size of  $20.1 \pm 0.2$  nm was correlated with a maximum H<sub>2</sub>  
 529 production rate. However, note the lower H<sub>2</sub> production rate observed below the optimum  
 530 anatase mean crystal size was caused by fast e<sup>-</sup>-h<sup>+</sup> recombination [57]. A decreasing H<sub>2</sub>  
 531 production rate which was correlated with fast e<sup>-</sup>-h<sup>+</sup> recombination at defective sites on the  
 532 photocatalyst surface [57]. The significantly great number of defective sites was due to  
 533 decreasing the crystal size below an optimum value.

534

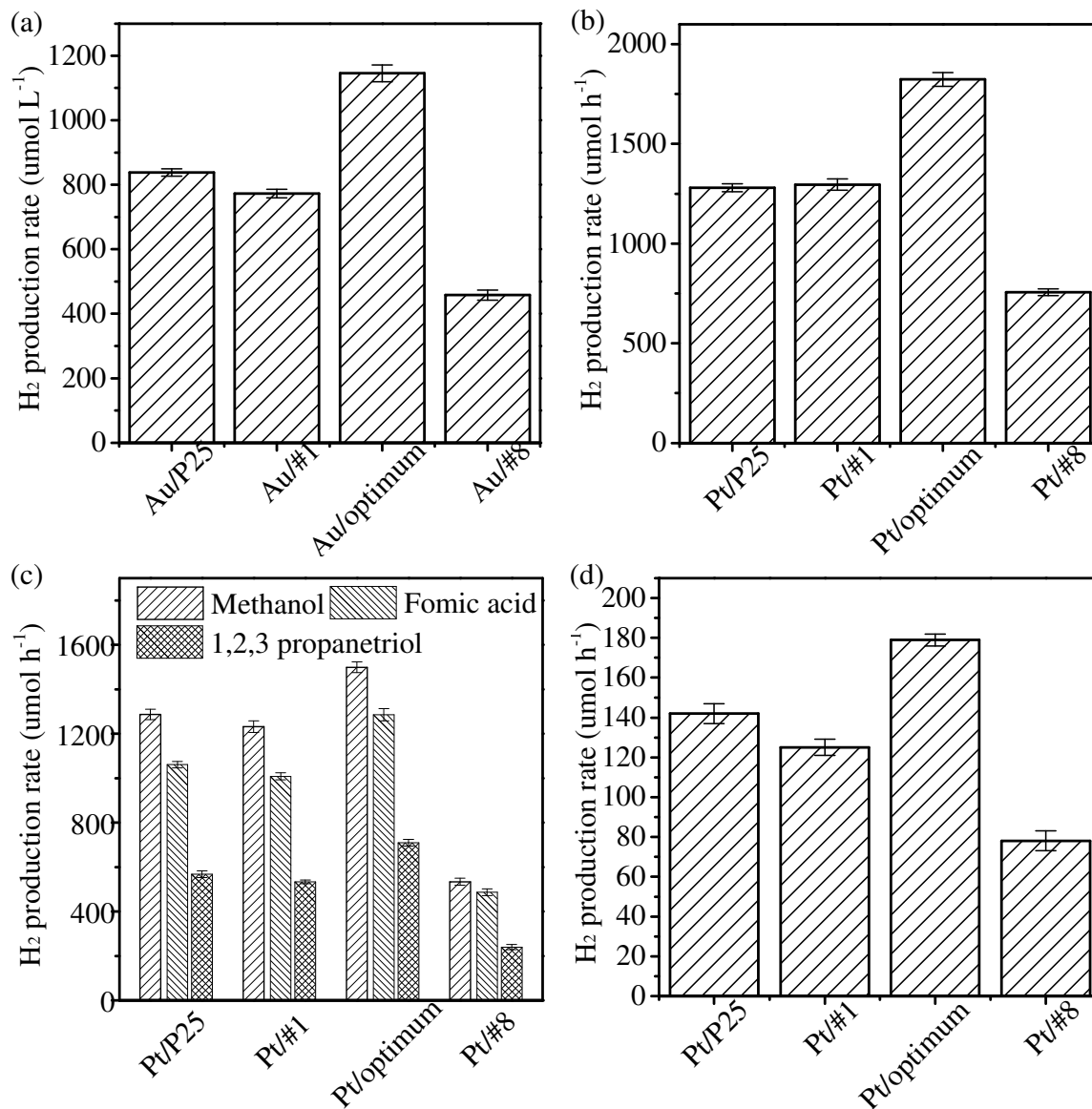
535

536

537 **3.8. Noble metal decorating and other alcohol sacrificial agents**

538 A significant increase in the H<sub>2</sub> production rate was observed when decorating the TiO<sub>2</sub>  
539 photocatalyst with Au or Pt (Figures 8a and b). The catalytic activity of the optimized 1D TiO<sub>2</sub>  
540 sample synthesized at 126°C, 15 M NaOH and 49 g·L<sup>-1</sup> TiO<sub>2</sub> was significantly enhanced by  
541 adding Au and Pt (Au/optimum or Pt/optimum) when compared to commercial TiO<sub>2</sub>  
542 nanoparticles decorated with Au or Pt (Au/P25 or Pt/P25). The catalytic activity of the optimized  
543 1D TiO<sub>2</sub> samples decorated with 2 wt% Au (Au/optimum) and Pt (Pt/optimum) were 1146±26  
544 μmol·h<sup>-1</sup> (ε = 48.7±1.1%) and 1823±35 μmol·h<sup>-1</sup> (ε = 77.5±1.5%), respectively. These rates were  
545 greater than those for other TiO<sub>2</sub> substrates decorated with 2 wt% of each metal. The Pt/optimum  
546 1D TiO<sub>2</sub> activity was greater when compared to the activity for the Au/optimum 1D TiO<sub>2</sub>  
547 photocatalyst. The H<sub>2</sub> production rate for Pt/optimum was approximately 5-fold greater when  
548 compared to the H<sub>2</sub> production rate (348 μmol·h<sup>-1</sup>) for TiO<sub>2</sub> nanotubes decorated with Pt  
549 nanoparticles [10].

550 Photocatalytic H<sub>2</sub> production studies were performed using the Pt/optimized 1D TiO<sub>2</sub> catalyst  
551 and different EDs (Figure 8c). The H<sub>2</sub> production rates were 1499±34 μmol·h<sup>-1</sup> (ε = 63.7±1.4%),  
552 1288±37 μmol·h<sup>-1</sup> (ε = 54.8±1.5%) and 710±15 μmol·h<sup>-1</sup> (ε = 30.2±0.6%) for methanol, formic  
553 acid and 1,2,3 propanetriol, respectively. In addition, under solar light conditions, the low H<sub>2</sub>  
554 production rate for the Pt/optimum 1D TiO<sub>2</sub> photocatalyst of 179±3 μmol·h<sup>-1</sup> (ε = 7.6±0.1%)  
555 (Figure 8d) was due to the low irradiation energy and the longer visible light wavelength when  
556 compared to only UV light.



557

558  
 559  
 560  
 561  
 562  
 563  
 564  
 565  
 566  
 567  
 568  
 569

Figure 8: H<sub>2</sub> production rate for (a) TiO<sub>2</sub> decorated with 2% Au under UV light condition, (b) TiO<sub>2</sub> decorated with 2% Pt under UV light condition, (c) Optimized 1D TiO<sub>2</sub> decorated with 2% Pt photocatalysts using methanol, formic acid and 1,2,3 propanetriol under UV light condition, and (d) TiO<sub>2</sub> decorated with 2% Pt using solar simulators.

Note: <sup>a</sup> Au/P25, Au/#1, Au/optimum and Au/#8 represent TiO<sub>2</sub> nanoparticles (P25), sample #1, optimized 1D TiO<sub>2</sub> and sample #8 decorated with 2% Au cocatalysts. <sup>b</sup> Pt/P25, Pt/#1, Pt/optimum and Pt/#8 represent P25, sample #1, optimized 1D TiO<sub>2</sub> and sample #8 decorated with Pt cocatalysts. <sup>c</sup>Optimum. represent optimized 1D TiO<sub>2</sub> synthesized at 126°C, 15 M NaOH and 49 g·L<sup>-1</sup> TiO<sub>2</sub>.

570 **4. Conclusion**

571 1D TiO<sub>2</sub> ranging from nanorods to nanowires were produced using a hydrothermal method  
572 with variable reaction conditions. The reaction temperature and NaOH concentration  
573 significantly affected the 1D TiO<sub>2</sub> phase structure, crystal size, SSA, bandgap energy and  
574 photocatalytic activity. A statistical model evaluated the effects of the hydrothermal synthesis  
575 factors on the photocatalytic activity of 1D TiO<sub>2</sub> in terms of the H<sub>2</sub> production rate. The AD and  
576 validation test indicated an adequate fit of the statistical model to the experimental data under the  
577 conditions examined. The model revealed that a relatively low temperature (126°C) and high  
578 NaOH concentration (15 M) were closely linked to producing 1D TiO<sub>2</sub> containing pure anatase.  
579 This 1D TiO<sub>2</sub> sample with an optimum mean crystal size was able to maximize the H<sub>2</sub>  
580 production rate. The 1D TiO<sub>2</sub> with biphasic anatase-rutile and anatase-TiO<sub>2</sub>-B structures was  
581 observed with decreasing photocatalytic H<sub>2</sub> production rate. A significant increase in the H<sub>2</sub>  
582 production rate was observed for the optimized 1D TiO<sub>2</sub> photocatalysts decorated with Pt or Au.  
583 This study demonstrated that 1D TiO<sub>2</sub> containing a controllable phase structure, and crystal size  
584 was able to produce a photocatalyst with a H<sub>2</sub> production rate greater than reported values.

585

586 **5. Acknowledgements**

587 Financial support for this work was provided by the Natural Sciences and Engineering  
588 Research Council (NSERC) of Canada (grant # 261797-2009), the Ontario Trillium scholarship  
589 program and the University of Windsor (grant #13320).

590

591 **6. Reference**

- 592 [1] P. Roy, S. Berger, P. Schmuki, TiO<sub>2</sub> nanotubes: synthesis and applications, *Angew. Chem.*  
593 *Int. Ed.* 50 (2011) 2904-2939.
- 594 [2] D.V. Bavykin, V.N. Parmon, A.A. Lapkin, F.C. Walsh, The effect of hydrothermal  
595 conditions on the mesoporous structure of TiO<sub>2</sub> nanotubes, *J. Mater. Chem.* 14 (2004) 3370-3378.
- 596 [3] H.Y. Zhu, Y. Lan, X.P. Gao, S.P. Ringer, Z.F. Zheng, D.Y. Song, J.C. Zhao, Phase transition  
597 between nanostructures of titanate and titanium dioxides via simple wet-chemical reactions., *J.*  
598 *Am. Chem. Soc.* 127 (2005) 6730-6736.
- 599 [4] X. Chen, S.S. Mao, Titanium dioxide nanomaterials: Synthesis, properties, modifications,  
600 and applications, *Chem. Rev.* 107 (2007) 2891-2959.
- 601 [5] B. Chen, J. Hou, K. Lu, Formation mechanism of TiO<sub>2</sub> nanotubes and their applications in  
602 photoelectrochemical water splitting and supercapacitors, *Langmuir* 29 (2013) 5911-5919.
- 603 [6] T. Kasuga, M. Hiramatsu, A. Hoson, T. Sekino, K. Niihara, Formation of titanium oxide  
604 nanotube, *Langmuir* 14 (1998) 3160-3163.
- 605 [7] Y. Tang, Y. Zhang, J. Deng, J. Wei, H.L. Tam, B.K. Chandran, Z. Dong, Z. Chen, X. Chen,  
606 Mechanical force-driven growth of elongated bending TiO<sub>2</sub>-based nanotubular materials for  
607 ultrafast rechargeable lithium ion batteries, *Adv. Mater.* 26 (2014) 6111-6118.
- 608 [8] Y.V. Kolen'ko, K.A. Kovnir, A.I. Gavrillov, Hydrothermal synthesis and characterization of  
609 nanorods of various titanates and titanium dioxide, *J. Phys. Chem. B* 110 (2006) 4030-4038.
- 610 [9] H.-W. Shim, D.K. Lee, I.S. Cho, K.S. Hong, D.-W. Kim, Facile hydrothermal synthesis of  
611 porous TiO<sub>2</sub> nanowire electrodes with high-rate capability for Li ion batteries, *Nanotechnology*  
612 21 (2010) 255706-255709.

- 613 [10] H.-L. Kuo, C.-Y. Kuo, C.-H. Liu, J.-H. Chao, C.-H. Lin, A highly active bi-crystalline  
614 photocatalyst consisting of TiO<sub>2</sub> (B) nanotube and anatase particle for producing H<sub>2</sub> gas from  
615 neat ethanol, *Catal. Lett.* 113 (2007) 7.
- 616 [11] A.R. Armstrong, G. Armstrong, J. Canales, P.G. Bruce, TiO<sub>2</sub>-B nanowires, *Angew. Chem.*  
617 116 (2004) 2336-2338.
- 618 [12] A. Kukovecz, K. Kordas, J. Kiss, Z. Konya, Atomic scale characterization and surface  
619 chemistry of metal modified titanate nanotubes and nanowires, *Surf. Sci. Rep.* 71 (2016) 473-  
620 546.
- 621 [13] J. Jitputti, S. Pavasupree, Y. Suzuki, S. Yoshikawa, Synthesis of TiO<sub>2</sub> nanotubes and its  
622 photocatalytic activity for H<sub>2</sub> evolution, *Jpn. J. Appl. Phys.* 47 (2008) 751.
- 623 [14] **T. Peng**, S. Ray, S.S. Veeravalli, J.A. Lalman, F. Arefi-Khonsari, The role of hydrothermal  
624 conditions in determining 1D TiO<sub>2</sub> nanomaterials bandgap energies and crystal phases, *Mater.*  
625 *Res. Bull.* 105 (2018) 104-113.
- 626 [15] T. Lavanya, M. Dutta, S. Ramaprabhu, K. Satheesh, Superior photocatalytic performance of  
627 graphene wrapped anatase/rutile mixed phase TiO<sub>2</sub> nanofibers synthesized by a simple and facile  
628 route, *J. Environ. Chem. Eng.* 5 (2017) 494-503.
- 629 [16] A.M. Hussein, L. Mahoney, R. Peng, H. Kibombo, C.-M. Wu, R.T. Koodali, R. Shende,  
630 Mesoporous coupled ZnO/TiO<sub>2</sub> photocatalyst nanocomposites for hydrogen generation, *J.*  
631 *Renew. Sustain. Ener.* 5 (2013) 033118.
- 632 [17] A.L. Linsebigler, G. Lu, J.T. Yates, Photocatalysis on TiO<sub>2</sub> surfaces: Principles,  
633 mechanisms, and selected results, *Chem. Rev.* 95 (1995) 735-758.



- 634 [18] J. Zhang, Q. Sun, J. Zheng, X. Zhang, Y. Cui, P. Wang, W. Li, Y. Zhu, The characterization  
635 of nitrogen doped TiO<sub>2</sub> photoanodes and its application in the dye sensitized solar cells, J.  
636 Renew. Sustain. Ener. 3 (2011) 033108.
- 637 [19] Q. Xiang, B. Cheng, J. Yu, Graphene based photocatalysts for solar fuel generation, Angew.  
638 Chem. 127 (2015) 11508-11524.
- 639 [20] X. Wang, K. Maeda, A. Thomas, K. Takanabe, G. Xin, J.M. Carlsson, K. Domen, M.  
640 Antonietti, A metal-free polymeric photocatalyst for hydrogen production from water under  
641 visible light, Nat. Mater. 8 (2008) 76-80.
- 642 [21] S.-W. Cao, Y.-P. Yuan, J. Fang, M.M. Shahjamali, F.Y.C. Boey, J. Barber, S.C.J. Loo, C.  
643 Xue, In-situ growth of CdS quantum dots on g-C<sub>3</sub>N<sub>4</sub> nanosheets for highly efficient  
644 photocatalytic hydrogen generation under visible light irradiation, Int. J. Hydrogen Energ. 38  
645 (2013) 1258-1266.
- 646 [22] M. Nasirian, M. Mehrvar, Modification of TiO<sub>2</sub> to enhance photocatalytic degradation of  
647 organics in aqueous solutions, J. Environ. Chem. Eng. 4 (2016) 4072-4082.
- 648 [23] A. Nada, M. Barakat, H. Hamed, N. Mohamed, T. Veziroglu, Studies on the photocatalytic  
649 hydrogen production using suspended modified photocatalysts, Int. J. Hydrogen Energ. 30 (2005)  
650 687-691.
- 651 [24] M. Murdoch, G.I.N. Waterhouse, M.A. Nadeem, J.B. Metson, M.A. Keane, R.F. Howe, J.  
652 Llorca, H. Idriss, The effect of gold loading and particle size on photocatalytic hydrogen  
653 production from ethanol over Au/TiO<sub>2</sub> nanoparticles, Nat. Chem. 3 (2011) 489-492.
- 654 [25] K. Connelly, A.K. Wahab, H. Idriss, Photoreaction of Au/TiO<sub>2</sub> for hydrogen production  
655 from renewables: a review on the synergistic effect between anatase and rutile phases of TiO<sub>2</sub>,  
656 Mater. Renew. Sustain. Ener. 1 (2012) 401-412.

- 657 [26] K. Hashimoto, H. Irie, A. Fujishima, TiO<sub>2</sub> photocatalysis: a historical overview and future  
658 prospects, *Jpn. J. Appl. Phys.* 44 (2005) 8269-8285.
- 659 [27] N. Qin, Y. Liu, W. Wu, L. Shen, X. Chen, Z. Li, L. Wu, One-dimensional CdS/TiO<sub>2</sub>  
660 nanofiber composites as efficient visible-light-driven photocatalysts for selective organic  
661 transformation: synthesis, characterization, and performance, *Langmuir* 31 (2015) 1203-1209.
- 662 [28] X. Wang, Z. Li, J. Shi, Y. Yu, One-dimensional titanium dioxide nanomaterials: Nanowires,  
663 nanorods, and nanobelts, *Chem. Rev.* 114 (2014) 9346-9384.
- 664 [29] J.B. Priebe, M. Karnahl, H. Junge, M. Beller, D. Hollmann, A. Brückner, Water reduction  
665 with visible light: synergy between optical transitions and electron transfer in Au-TiO<sub>2</sub> catalysts  
666 visualized by in situ EPR spectroscopy, *Angew. Chem. Int. Ed.* 52 (2013) 11420-11424.
- 667 [30] G. Xie, K. Zhang, B. Guo, Q. Liu, L. Fang, J.R. Gong, Graphene-based materials for  
668 hydrogen generation from light-driven water splitting, *Adv. Mater.* 25 (2013) 3820-3839.
- 669 [31] V.M. Daskalaki, D.I. Kondarides, Efficient production of hydrogen by photo-induced  
670 reforming of glycerol at ambient conditions, *Catal. Today* 144 (2009) 75-80.
- 671 [32] N. Strataki, V. Bekiari, D.I. Kondarides, P. Lianos, Hydrogen production by photocatalytic  
672 alcohol reforming employing highly efficient nanocrystalline titania films, *Appl. Catal., B*  
673 *Environ.* 77 (2007) 184-189.
- 674 [33] S. McAllister, J.-Y. Chen, A.C. Fernandez-Pello, *Fundamentals of Combustion Processes*,  
675 Springer Science & Business Media, New York, NY, 2011.
- 676 [34] K. Zhang, Q. Liu, H. Wang, R. Zhang, C. Wu, J.R. Gong, TiO<sub>2</sub> single crystal with four-  
677 truncated-bipyramid morphology as an efficient photocatalyst for hydrogen production, *Small* 9  
678 (2013) 2452-2459.

- 679 [35] S. Ray, J.A. Lalman, N. Biswas, Using the Box-Benken technique to statistically model  
680 phenol photocatalytic degradation by titanium dioxide nanoparticles, *Chem. Eng. J.* 150 (2009)  
681 15-24.
- 682 [36] J. Liu, Y. Liu, N. Liu, Y. Han, X. Zhang, H. Huang, Y. Lifshitz, S.T. Lee, J. Zhong, Z. Kang,  
683 Metal-free efficient photocatalyst for stable visible water splitting via a two-electron pathway,  
684 *Science* 347 (2015) 970-974.
- 685 [37] S.S. Veeravalli, S.R. Chaganti, J.A. Lalman, D.D. Heath, Optimizing hydrogen production  
686 from a switchgrass steam exploded liquor using a mixed anaerobic culture in an upflow  
687 anaerobic sludge blanket reactor, *Int. J. Hydrogen Energ.* 39 (2014) 3160-3175.
- 688 [38] S.R. Shanmugam, S.R. Chaganti, J.A. Lalman, D.D. Heath, Statistical optimization of  
689 conditions for minimum H<sub>2</sub> consumption in mixed anaerobic cultures: effect on  
690 homoacetogenesis and methanogenesis, *Int. J. Hydrogen Energ.* 39 (2014) 15433-15445.
- 691 [39] Y.-C. Pu, Y.-C. Chen, Y.-J. Hsu, Au-decorated Na<sub>x</sub>H<sub>2-x</sub>Ti<sub>3</sub>O<sub>7</sub> nanobelts exhibiting  
692 remarkable photocatalytic properties under visible-light illumination, *Appl. Catal., B Environ.* 97  
693 (2010) 389-397.
- 694 [40] J. Zhang, Q. Xu, Z. Feng, M. Li, C. Li, Importance of the relationship between surface  
695 phases and photocatalytic activity of TiO<sub>2</sub>, *Angew. Chem. Int. Ed.* 47 (2008) 1766-1769.
- 696 [41] T. Kogure, T. Umezawa, Y. Kotani, A. Matsuda, M. Tatsumisago, T. Minami, Formation of  
697 TiO<sub>2</sub>(B) nanocrystallites in sol - gel - derived SiO<sub>2</sub> - TiO<sub>2</sub> film, *J. Am. Ceram. Soc.* 82 (1999)  
698 3248-3250.
- 699 [42] Y.Q. Wang, G.Q. Hu, X.F. Duan, H.L. Sun, Q.K. Xue, Microstructure and formation  
700 mechanism of titanium dioxide nanotubes, *Chem. Phys. Lett.* 365 (2002) 427-431.

701 [43] A. Chemseddine, T. Moritz, Nanostructuring titania: control over nanocrystal structure, size,  
702 shape, and organization, *Eur. J. Inorg. Chem.* 1999 (1999) 235-245.

703 [44] G.L. Chiarello, E. Selli, L. Forni, Photocatalytic hydrogen production over flame spray  
704 pyrolysis-synthesised TiO<sub>2</sub> and Au/TiO<sub>2</sub>, *Appl. Catal., B Environ.* 84 (2008) 332-339.

705 [45] Z. Lai, M. Zhu, X. Yang, J. Wang, S. Li, Optimization of key factors affecting hydrogen  
706 production from sugarcane bagasse by a thermophilic anaerobic pure culture, *Biotechnol.*  
707 *Biofuels* 7 (2014) 131-111.

708 [46] A. Reungsang, S. Pattra, S. Sittijunda, Optimization of key factors affecting methane  
709 production from acidic effluent coming from the sugarcane juice hydrogen fermentation process,  
710 *Energies* 5 (2012) 4746-4757.

711 [47] M.A. Stephens, EDF statistics for goodness of fit and some comparisons, *J. Am. Stat. Assoc.*  
712 69 (1974) 730.

713 [48] H. Cheng, J. Ma, Z. Zhao, L. Qi, Hydrothermal preparation of uniform nanosize rutile and  
714 anatase particles, *Chem. Mater.* 7 (1995) 663-671.

715 [49] H. Zhang, J.F. Banfield, Understanding polymorphic phase transformation behavior during  
716 growth of nanocrystalline aggregates: insights from TiO<sub>2</sub>, *J. Phys. Chem. B* 104 (2000) 3481-  
717 3487.

718 [50] M.C. Hidalgo, M. Maicu, J.A. Navío, G. Colón, Photocatalytic properties of surface  
719 modified platinised TiO<sub>2</sub>: effects of particle size and structural composition, *Catal. Today* 129  
720 (2007) 43-49.

721 [51] G. Tian, H. Fu, L. Jing, B. Xin, K. Pan, Preparation and characterization of stable biphasic  
722 TiO<sub>2</sub> photocatalyst with high crystallinity, large surface area, and enhanced photoactivity, *J. Phys.*  
723 *Chem. C* 112 (2008) 3083-3089.

- 724 [52] A. Monshi, M.R. Foroughi, M.R. Monshi, Modified Scherrer equation to estimate more  
725 accurately nano-crystallite size using XRD, *World J. Nano Sci. Eng.* 02 (2012) 154-160.
- 726 [53] H. Luo, C. Wang, Y. Yan, Synthesis of mesostructured titania with controlled crystalline  
727 framework, *Chem. Mater.* 15 (2003) 3841-3846.
- 728 [54] R. Lopez, R. Gomez, Band-gap energy estimation from diffuse reflectance measurements on  
729 sol-gel and commercial TiO<sub>2</sub>: a comparative study, *J. Sol-Gel Sci. Technol.* 61 (2012) 1-7.
- 730 [55] J. Tao, T. Luttrell, M. Batzill, A two-dimensional phase of TiO<sub>2</sub> with a reduced bandgap,  
731 *Nat. Chem.* 3 (2011) 296-300.
- 732 [56] W. Fan, Q. Lai, Q. Zhang, Y. Wang, Nanocomposites of TiO<sub>2</sub> and reduced graphene oxide  
733 as efficient photocatalysts for hydrogen evolution, *J. Phys. Chem. C* 115 (2011) 10694-10701.
- 734 [57] I. Okura, M. Kaneko, *Photocatalysis science and technology*, Springer and Kodansha, Japan,  
735 2002.
- 736
- 737

1  
2  
3  
4  
5  
6

# Optimizing one-dimensional TiO<sub>2</sub> for photocatalytic hydrogen production from a water-ethanol mixture and other electron donors

Tao Peng, Jian Zhang, Srimanta Ray, Fatemeh Saadat Ghareh Bagh, Houssam Fakhouri, Farzaneh Arefi-Khonsari and Jerald A. Lalman

